



Fault geometry and low frictional control of the near-field postseismic deformation of the 2021 Mw 7.3 Maduo earthquake

Lei Zhao ^{a,b}, Wenbin Xu ^{a,b,*}, Lei Xie ^{a,b}, Dezheng Zhao ^c, Zhihui Zhu ^d, Pingping Wu ^e, Huili Guo ^e

^a Key Laboratory of Metallogenetic Prediction of Nonferrous Metals and Geological Environment Monitoring, Central South University, Ministry of Education, Changsha 410000, China

^b School of Geosciences and Info-Physics, Central South University, Changsha, China

^c State Key Laboratory of Earthquake Dynamics, Institute of Geology, China Earthquake Administration, Beijing 100029, China

^d School of Civil Engineering, Central South University, Changsha, China

^e Institute of Geophysics, China Earthquake Administration, Beijing 100081, China

ARTICLE INFO

Keywords:

Fault bending
Friction parameter
Postseismic deformation
Maduo earthquake
Dynamic weakening

ABSTRACT

The 2021 Maduo earthquake caused ~160 km-long complex coseismic surface rupture and postseismic deformation. However, the afterslip pattern and primary reason for the overlapped coseismic slip and afterslip in shallow portion in Maduo earthquake are still unclear. Here, we used ~0.85 yr Sentinel-1 data to obtain the time-dependent postseismic deformation of the 2021 Mw 7.3 Maduo earthquake and inverted afterslip distribution. We calculated the frictional parameter of the seismogenic fault based on the time series afterslip and depicted the rupture surface based on three-dimensional coseismic displacement. Our findings indicated that the more considerable postseismic deformation in the near-field was concentrated on the bending region near the epicenter. The maximum afterslip was ~0.35 m in the shallow upper crust. The shallow afterslip overlapped with the coseismic rupture, mainly caused by the low frictional parameter ($a - b = 0.002$) and shear heating in the shallow region. The fault geometry was gentle in the supershear rupture area, while changed substantially in the west of the epicenter. This highlights that the fault bending could have controlled both coseismic and postseismic deformation pattern in near-field. It also indicates that fault bending controls the stress propagation for large strike-slip fault, which provides a new perspective for seismic risk assessment of other strike-slip faults in the Bayan Har block.

1. Introduction

In the past 20 years, several moderate-to-strong earthquakes have occurred around the Bayan Har block (Fig. 1b). On May 21, 2021, the Mw 7.3 earthquake occurred in Maduo (Qinghai, China), located on the Kunlunshankou-Jiangcuo fault within the Bayan Har block (Pan et al., 2021). Previous studies reflected the complex rupture characteristics and heterogeneous coseismic slips implicate the lateral inhomogeneity of the frictional property along the rupture fault (Zhao et al., 2021; Yue et al., 2022). The coseismic slip models based on the Interferometric Synthetic Aperture Radar (InSAR) data showed a shallow slip with heterogeneous slip distribution along the fault and slip deficit areas (Zhao et al., 2021; He et al., 2021; Jin and Fialko, 2021). The back projection images based on the teleseismic data indicate a high speed (i.

e., supershear or sub-shear speed) propagation of the fault rupture on the east side of the epicenter (Chen et al., 2022; Xu et al., 2020; Yue et al., 2022; Zhang et al., 2022). The surface ruptures mapped from Unmanned Aerial Vehicle (UAV) imagery and InSAR data showed a bilateral propagation of ~160 km length (Yuan et al., 2022; Liu et al., 2022). Two rupture gaps in the fault surface trace were located in the desert and swamp areas (Yuan et al., 2022; Liu et al., 2022). The unfavorable landscape features (e.g., desert and wetland) may affected the observation of the UAV, rendering it difficult to find the obvious fault surface trace. As the fault geometry was crucial in controlling rupture and deformation, which may be the main factor causing the difference in the rupture velocity on the east and west sides (Fig. 1d) of the epicenter to control the deformation pattern, a detailed fault geometry should be elaborated.

* Corresponding author at: Key Laboratory of Metallogenetic Prediction of Nonferrous Metals and Geological Environment Monitoring, Central South University, Ministry of Education, Changsha 410000, China.

E-mail address: wenbin.xu@csu.edu.cn (W. Xu).

Previous studies of the early afterslip showed different results. Wang et al. (2022) reported noticeable shallow afterslip in the early 24 d and overlapped with the coseismic slip, while He et al. (2021) suggested that the afterslip was mainly distributed in the deep, and partly overlapped with the coseismic slip in the shallow region. They explained the shallow afterslip as a stress-driven process due to the Coulomb stress loading from coseismic slip. Jin and Fialko (2021) indicated that the shallow afterslip made up for parts of the coseismic shallow slip deficit. Xiong et al. (2022) jointly inverted the InSAR and GPS observation, and suggested that the afterslip overlapped with the coseismic slip in the shallow portion, and considered the coseismic slip propagated through the velocity-strengthening body. However, due to the short period of the observation time, the previous studies only presented preliminary afterslip model and not examined the frictional property of the seismogenic fault, and lacked the further research on the postseismic deformation mechanism and spatiotemporal distribution of the afterslip. Hence, the distribution of the afterslip and formation of the overlapping region in the shallow region was still unclear. In addition, possible reasons such as dynamic weakening (Noda and Lapusta, 2013) and fault heterogeneity of velocity-strengthening body should be future determined to provide a better constrains of fault property and afterslip behaviour.

Therefore, different from the previous studies of the Maduo

earthquake, this study concentrates on exploring the critical factors for the formation of the shallow afterslip and rupture characteristics based on long-term observation data, and explore the key factors of the near-field postseismic deformation through the frictional properties and geometric structure of the seismogenic fault. We interpreted the postseismic deformation through afterslip, poroelastic and viscoelastic mechanisms. We depicted the surface trace to observe the fault strike variation and discussed the relationship between the fault geometry and the near-field postseismic deformation.

2. Modeling and results

2.1. Time series postseismic deformation

To observe the spatiotemporal postseismic deformation characteristics and probe the seismogenic fault frictional property, we processed the ~0.85 yr descending and ascending Sentinel-1A/B data. Interferograms were calculated using multilook factors of 10 and 2 in the range and azimuth directions, respectively, to improve the signal-to-noise ratio (SNR). A Shuttle Radar Topography Mission (SRTM)-90 digital elevation model was used to correct the topographic phase. We masked out the pixel with a coherence lower than 0.5 and removed the interferograms with perpendicular baseline >50 m; the spatiotemporal

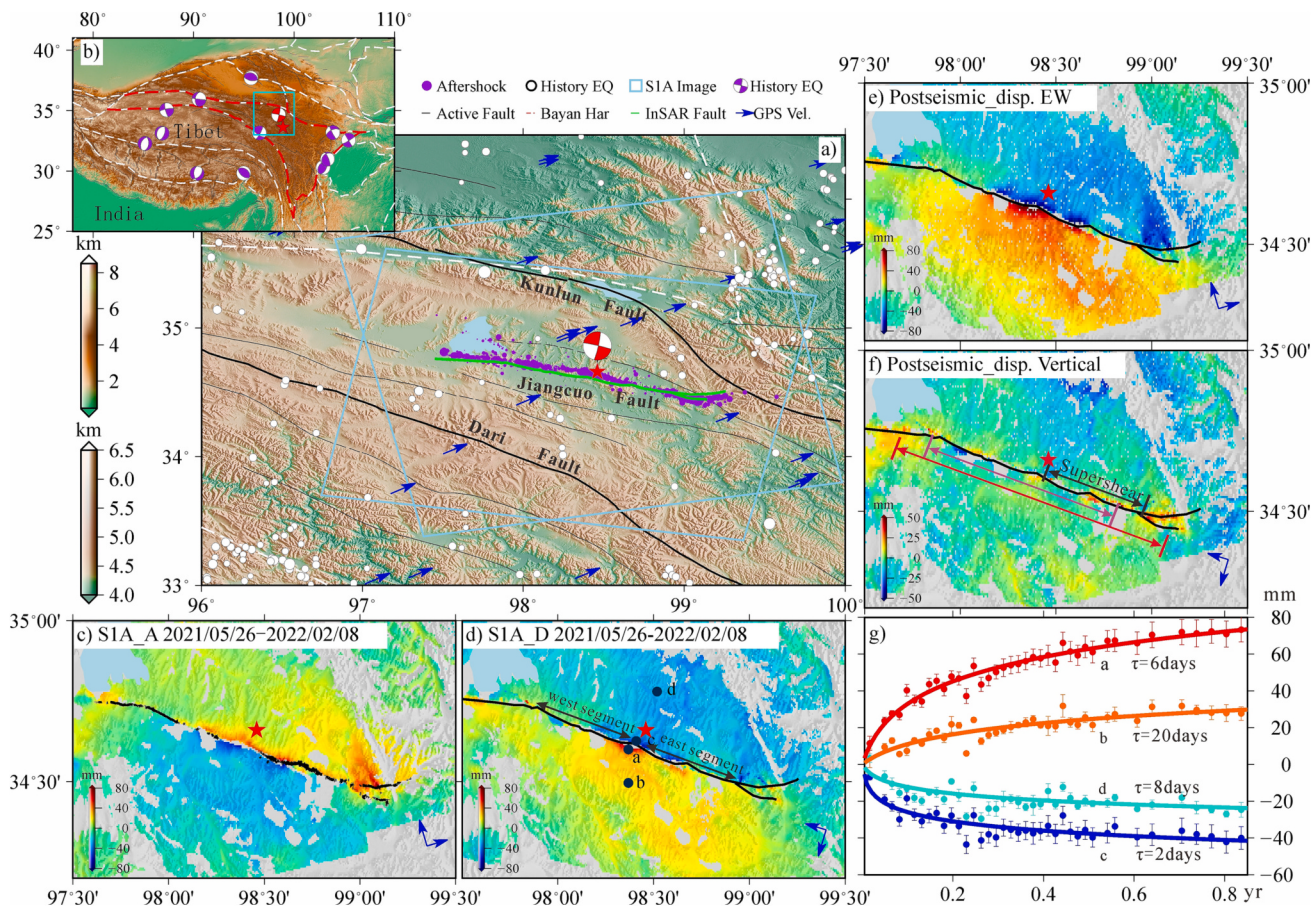


Fig. 1. (a) Tectonic setting of the Maduo earthquake. Green solid line denotes the surface rupture trace from the InSAR data. Black solid lines represent active faults. The purple circles represent the relocated aftershocks (Wang et al., 2021). Blue arrows represent the interseismic GPS velocities (Wang and Shen, 2020). White circles represent the history earthquakes. The cyan boxes show the ascending and descending image. (b) Tectonic setting of the Tibetan Plateau. Red dotted line marks the Bayan Har block. The red focal mechanism solution represents the Maduo earthquake. The purple focal mechanism solution represents the history earthquake. (c) Cumulative postseismic deformation of the ascending orbit. The black line denotes the rupture trace from UAV photography (Liu-Zeng et al., 2022). (d) Cumulative postseismic deformation of the descending orbit. (e, f) The decomposed east-west and vertical postseismic deformation using the cumulative deformation of (c, d). The black bidirectional arrow denotes the supershear area. The red bidirectional arrow denotes the area of Fig. 3. The purple bidirectional arrow denotes the area of Fig. 5. (g) Time series postseismic deformation of four feature points in (d). (For interpretation of the references to colour in this figure legend, the reader is referred to the web version of this article.)

baseline network diagrams of both orbitals are shown in Fig. S1. The interferograms filtered by the adaptive filter (Goldstein and Werner, 1998) and obtained the unwrapping interferograms based on the minimum cost flow (MCF) method (Werner et al., 2000). All the pre-processing was carried out by the GAMMA software. We then used the open-source software LiCSBAS 7.0 (Morishita et al., 2020) to conduct time series analysis based on the N-SBAS method. First, we calculated phase closure of interferogram triplets, and remove the images which the loop closure phase >1.5 rad. Subsequently, we calculated the standard deviation (STD) of the velocity and masked the area with low coherence and high STD. Finally, we applied a high-pass in time and low-pass in space with the gaussian kernel and obtained the time-series postseismic deformation.

To measure the E-W and vertical postseismic deformation, we used two-dimensional decomposition by combining the ascending and descending postseismic interferograms. The $D_{los}D_{los}$ can be expressed as:

$$D_{los} = D_u * \cos\theta - D_e * \sin\theta * \cos\phi \quad (1)$$

where D_e and D_u represent the E-W and vertical displacement components, respectively. Los represents the line-of-sight deformation. θ is the incidence angle of the pixel, ϕ is the azimuth of the satellite heading vector.

The ascending and descending InSAR observations indicated similar postseismic deformation pattern with the coseismic deformation (Fig. 1c, d). The two-dimensional postseismic deformation (Fig. 1e, f) represented sinistral strike-slip motion in agreement with the slip behaviour of the seismogenic fault. Two obvious deformation regions were distributed in the near-field of the seismogenic fault, and the line of sight (LOS) deformation value in the near-field (~ 80 mm) was twice than that of the far-field (~ 40 mm). Four feature points were selected to observe the different decay velocity between the near-field and far-field deformation (Fig. 1g). The decay coefficient of the time-series observation fitted with the formulation:

$$F = a \times \log(1 + T/\tau) \quad (2)$$

where a represents the scaling factor, T is the measurement time, τ represents the decay coefficient. The decay velocity of the near-field (6 d) was faster than that of the far-field (20 d), indicating different frictional properties of the seismogenic fault in the shallow and deep regions.

2.2. Postseismic afterslip model

The afterslip is generally the primary deformation mechanism for the early postseismic deformation. We combined the kinematic afterslip with stress-driven afterslip to observed the spatiotemporal afterslip distribution characteristic. The kinematic afterslip can intuitively reflected the first-order characteristic but not the physical mechanism of the afterslip. The stress-driven afterslip is physically plausible and is an important way to probe the frictional property (Barbot et al., 2009). To observe the spatiotemporal kinematic afterslip distribution, we used the steepest descent method (SDM, Wang et al., 2013) to observe the kinematic afterslip distribution. We used Yue et al. (2022) coseismic slip model and extended the fault width to 30 km, which was constrained by the InSAR, GPS and telesismic data. The fault geometry determined by the surface rupture trace and dipped to north with a dip angle of 83° . The coseismic slip was mainly distributed in the shallow portion with a maximum slip of ~ 5 m. We set the rake angle in -45° – 45° according to the left-lateral deformation characteristic.

For the stress-driven afterslip model, we used the open-source program RELAX to forward simulate the postseismic deformation, which evaluated the nonlinear time-dependent displacement for the rate-strengthening friction on faults where loading Coulomb stress (Barbot et al., 2009).

We searched for the optimal values of V_0 and $(a - b)\sigma$ in the ranges of

$2\text{--}10$ m/yr and $2\text{--}10$ MPa based on the RMS between the forward modeling data and the time-series InSAR observation. V_0 is the reference slip rate of the time scale afterslip, $(a - b)$ represents the frictional parameter of the rock, and σ is the effective normal stress on the fault.

The kinematic afterslip was mainly distributed in the deep part (16–24 km), the shallow part near the epicenter (0–4 km), and the lateral extension area of the seismogenic fault (Fig. 2a). The maximum afterslip in the shallow and deep regions was ~ 0.35 m and ~ 0.4 m, respectively, in ~ 0.85 yr after the mainshock. The total moment released by the early afterslip was $\sim 1.799 \times 10^{19}$ Nm corresponding to a magnitude of Mw 6.77 ($\sim 11.4\%$ of the mainshock). The optimal value of $V_0 = 3$ m/yr and $(a - b)\sigma = 6$ MPa were found when RMS was the lowest (Fig. S5). The stress-driven afterslip was mainly distributed in the deep region of the seismogenic fault, with almost no afterslip in the shallow region (Fig. 2b). The maximum stress-driven afterslip in the deep portion was ~ 0.6 m. The forward deformation can fit the far-field deformation, while the near-field deformation cannot be fitted completely (Fig. 3). The deviation between the forward and observed data in the near-field was mainly due to the simplification of the coseismic slip model, especially for the complex fault geometry event. The forward deformation in the far-field can restore part of the observation, while the residual deformation maybe the contribution of the viscoelastic relaxation. The tradeoff between the afterslip and viscoelastic relaxation should be studied in future research.

We used Coulomb 3.3 to calculate the coseismic static stress change on the fault plane (Fig. 2d). The afterslip is usually distributed in the coseismic static Coulomb stress loading area (Wallace et al., 2018; Dogan et al., 2014). Afterslip, aftershocks, and coseismic slip formed a good spatial complementarity. Aftershocks were mainly distributed in the region between coseismic slip and afterslip filling up the slip deficit, and the deep afterslip was mainly distributed in the Coulomb stress loading area.

2.3. Poroelastic rebound model

The changed in the pore pressure caused by coseismic stress and the fluid-pressure re-equilibration in the postseismic period can induced obvious deformation in the surface. For the early postseismic period, poroelastic rebound played an important role in controlling near-field deformation. We usually observing the difference in the coseismic deformation in the drain and undrained condition via changes the Poisson's ratio in elastic dislocation models. In this study, we used Wang and Kümpel (2003) method to set up the multi-layer half-space model according to the Crust 1.0 model and constructing the Green's functions based on the flexible structure (V_p and V_s) and the hydraulic diffusivity for each layer to realize the drain and undrained condition (Bevis et al., 2015). We set the hydraulic diffusivity separately to $0.5 \text{ m}^2/\text{s}$ and $1 \text{ m}^2/\text{s}$ to simulate the postseismic deformation.

The simulated deformation presents a four-quadrant distribution (Fig. 4). The simulated deformation magnitude was much less than the observation in the two bend regions. The obvious simulated deformation was in the eastern end but was contrary to the observation. Thus, the poroelastic rebound was not the deformation mechanism for the near-field deformation.

2.4. Viscoelastic relaxation

Viscoelastic relaxation is a major factor of postseismic deformation. Here, we used crust model that considered the different rheology between the lower crust and upper mantle (Fig. S6). We used the Psgrn/Pscmp code (Wang et al., 2021) to model viscoelastic relaxation following the Maduo earthquake based on the Burgers body rheology. We set the transient viscosity (η_k) and steady viscosity (η_m) for both lower crust and upper mantle (Fig. S6). The results showed that the simulated deformation was mainly distributed in the far-field. The maximum postseismic deformation in the far-field was ~ 10 mm in one

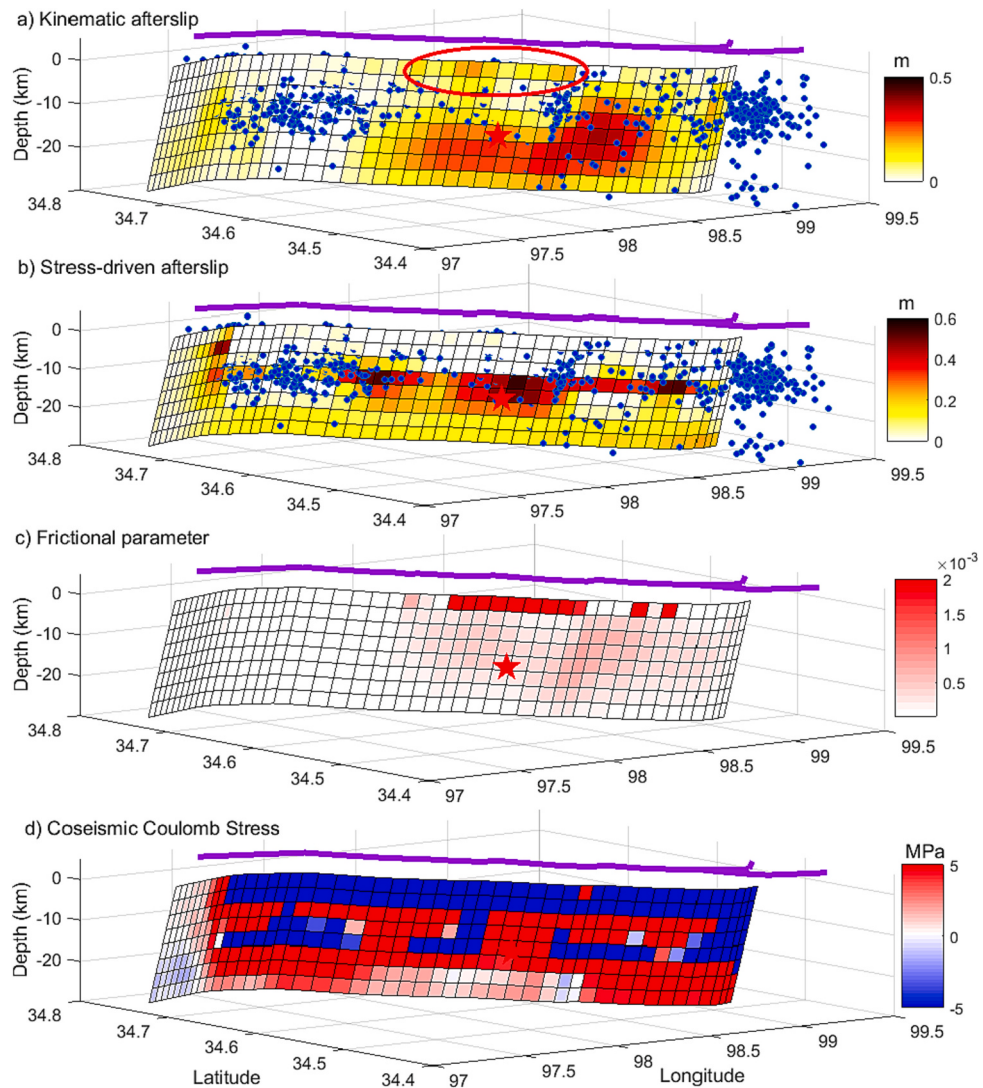


Fig. 2. a), b) Kinematic afterslip and stress-driven distribution model in the first 264 days after the mainshock. Red ellipse denotes the shallow overlapped afterslip region. c) The distribution of friction parameter ($a - b$) on the seismogenic fault. d) Coseismic Coulomb stress change. The red star represents the epicenter, the blue dots denote the relocated aftershocks. The purple line represents the rupture trace.

year when we set $\eta_{k1} = 10^{17}$ Pa S, $\eta_{m1} = 10^{18}$ Pa S for lower crust. While negligible deformation was seen in the near-field comparing to the data, we excluded that the possibility of viscoelastic relaxation as the dominant factor.

2.5. Rupture surface trace

To observe the relation between rupture velocity, deformation pattern, and fault geometry, we computed the curl, divergence, and shear strain to extract the surface rupture trace based on the E-W and N-S coseismic deformation (Zhou et al., 2018a, 2018b; Liu et al., 2022). A positive value of divergence indicated extension, and a positive value of the curl denoted the left lateral strike slip rupture (Zhou et al., 2018a, 2018b). The shear strain indicated the variation of the angle between NS and EW displacement, positive and negative values represent the left-lateral and right-lateral strike slips, respectively (Li et al., 2020). The curl ω , divergence δ , and shear strain γ were obtained as follows:

$$\omega = (\nabla \times \vec{F})_z = \frac{\partial_v}{\partial_x} - \frac{\partial_u}{\partial_y} \quad (3)$$

$$\delta = (\nabla_h \times \vec{F}) = \frac{\partial_u}{\partial_x} + \frac{\partial_v}{\partial_y} \quad (4)$$

$$\gamma = (\Delta \times \vec{F})_z = \frac{\partial_v}{\partial_x} + \frac{\partial_u}{\partial_y} \quad (5)$$

where \vec{F} represents the displacement field, u and v represent the EW and NS displacement respectively. x is the east-west and y is the south-north direction.

The fault surface trace obtained based on divergence and curl perfectly made up for the gap observed by UAV, and showing obvious lateral inhomogeneity (Fig. S7). The results in agreement with the UAV observation (Fig. 1d), which indicated the reliability of the divergence. Two obvious bending regions existed on the surface trace, one was located on the east of the epicenter, and another near the epicenter. We calculated the strike angle variation of the surface rupture trace. It can be seen that the strike changes sharply in the west side of the epicenter from 270° to 310° , and there were several places where the strike angle changes instantaneously, while the strike changes gently in the east side of the epicenter around 280° (Fig. 6a).

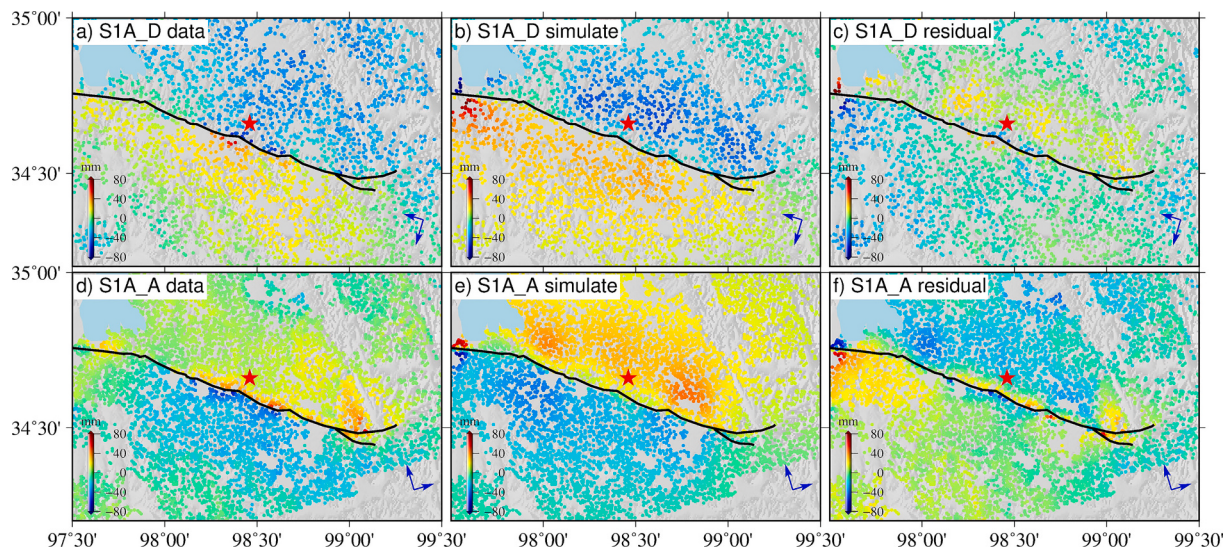


Fig. 3. Simulated postseismic deformation of the stress driven afterslip. The red star represents the epicenter. The black solid represents the InSAR rupture surface. (For interpretation of the references to colour in this figure legend, the reader is referred to the web version of this article.)

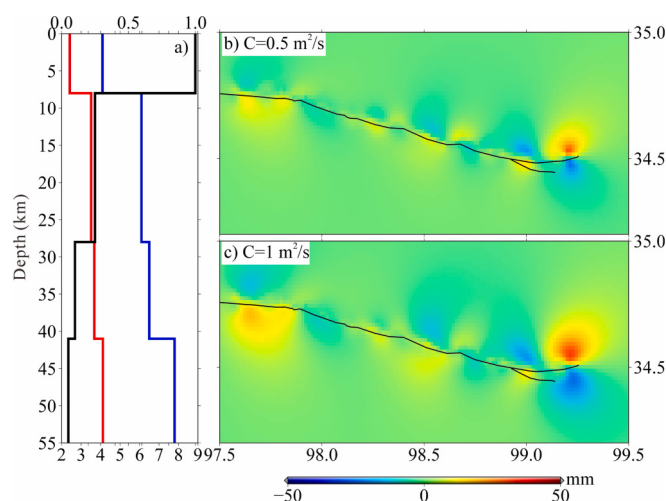


Fig. 4. a) Multilayered earth structure used in this study of time-dependent poroelastic rebound displacements. b), c) The simulated descending post-seismic deformation of poroelastic rebound with hydraulic diffusivity for $0.5 \text{ m}^2/\text{s}$ and $1 \text{ m}^2/\text{s}$ respectively.

3. Discussion

3.1. Reliability of the afterslip distribution

The unruptured and slip deficit regions around the coseismic slip are either velocity-strengthening bodies or velocity weakening bodies, in which stress does not reach the rupture threshold (Yamanaka and Kikuchi, 2004; Miyazaki et al., 2004). Therefore, the rupture behaviour of slip deficit region and unruptured region in the postseismic period are of great significance to distinguish physical properties of the seismogenic fault. The deep kinematic afterslip was distributed in several continuous velocity-strengthening bodies, while the shallow kinematic afterslip distribution was more discrete. Part of the shallow kinematic afterslip was located on the regions with large coseismic slip, which may be affected by the downsampling and smoothing factor. We test the reliability of the kinematic afterslip model using jackknife resampling technique (Melgar et al., 2015). Fifty percent of downsampled InSAR data were randomly removed, and we regenerated the slip model using the remaining data. After one inversion was completed, the removed data was returned to the data pool and the process was repeated by eliminating another 50% of the data. We repeated this 50 times and then calculated the standard deviations of each patch of the model. The maximum standard deviation of the slip model was $\sim 0.02 \text{ m}$ (Fig. S8a), accounting for only $\sim 5\%$ of the afterslip. Furthermore, different smoothing factors of the model showed a similar slip pattern (Fig. S8).

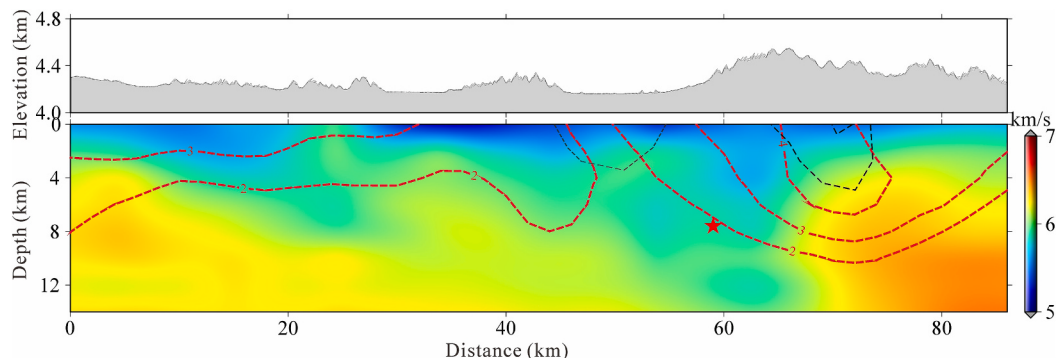


Fig. 5. The velocity profile along the jiangcuo fault. The red dotted contour lines represent the coseismic slip. The black dotted contour lines represent the post-seismic slip. The red star represents the epicenter. (For interpretation of the references to colour in this figure legend, the reader is referred to the web version of this article.)

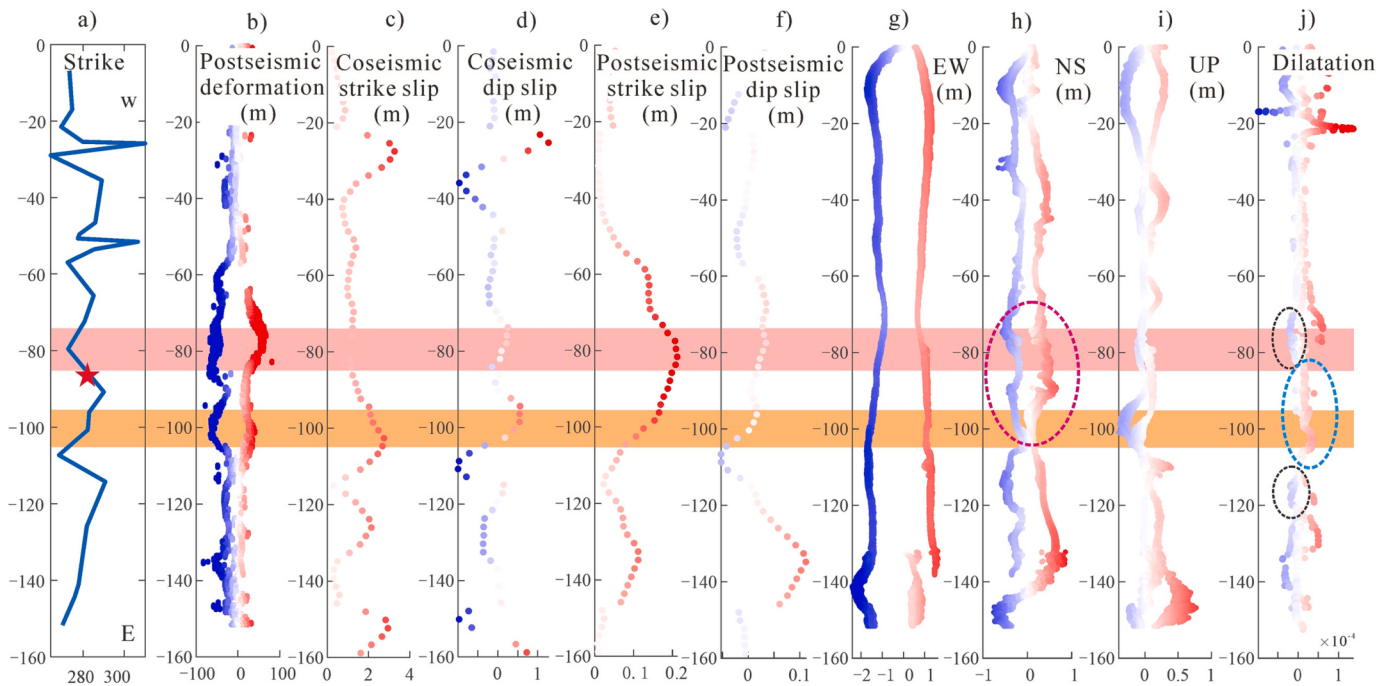


Fig. 6. Relationship between the fault geometry and deformation. From left to right. a) Fault strike from west to east. b) Postseismic deformation profiles along the strike in near-field. c) Averaged coseismic strike slip profiles along the strike (Yue et al., 2022). d) Averaged coseismic dip slip (Yue et al., 2022). e) Averaged postseismic strike slip. f) Averaged postseismic dip slip. g) Coseismic deformation in EW component in near-field (Liu et al., 2022). h) Coseismic deformation in NS component in near-field (Liu et al., 2022). i) Coseismic deformation in vertical component in near-field (Liu et al., 2022). j) Dilatation variation (Liu et al., 2022). The pink and orange bar highlights the large near-field postseismic deformation area. The red star represents the epicenter. The black dotted oval represents the compression area. The cyan dotted oval represents the tension area. The pink dotted oval represents the tension deformation. The range of the profile is shown in Fig. 1f red oval. (For interpretation of the references to colour in this figure legend, the reader is referred to the web version of this article.)

These experiments lead us to conclude that our kinematic afterslip model was well constrained by InSAR observations.

For coseismic slip shallow deficit, it is more severe for immature seismogenic faults, which can be observed in many strike-slip faults (Chorsi et al., 2022; Fialko et al., 2005). Jin and Fialko (2021) suggested the shallow slip deficit is of the order of 30%. Our results show that the shallow kinematic afterslip is only ~0.35 m within ~0.85 yr after the earthquake, which was far from compensating for the shallow slip deficit. Li et al., (2023) showed that >80% of the displacement occurred as off-fault deformation based on the Sentinel-2 data, the partial inelastic deformation may compensate for part of the shallow slip deficit. The shallow slip deficit may be finally compensated by off-fault deformation during interseismic (Chorsi et al., 2022), therefore, the continuous deformation observation was of great significance for the study of fault maturity.

3.2. Frictional properties of the seismogenic fault

The logarithmic time evolution of the afterslip reflect the logarithmic dependence of the friction for the creeping fault (Avouac, 2015). In order to directly observed the difference of frictional properties between the shallow and deep region of the seismogenic fault, we calculated the frictional parameter of the seismogenic fault. We obtained the time series postseismic slip model ($S(t) = A^* \ln(1 + t/\tau)$) based on the InSAR observation. Based on the rate-and-state friction laws, it can be equivalent to $S(t) = \frac{\sigma(a-b)}{k} * \ln\left(1 + \frac{kv}{\sigma(a-b)}t\right)$ (Scholz, 2002). Therefore $a - b = Ak/\sigma$, and σ is the effective normal stress. Assuming the fluid pressure to be 0, the effective normal stress can be expressed as $\sigma = \rho gh^* \cos(dip)$ (Zhou et al., 2018a, 2018b), where ρ represents the density of the crustal rock (in this paper, $\rho = 2700 \text{ kg/m}^3$, $g = 9.8 \text{ m/s}^2$), h and dip denote the depth and dip of each sub-patches respectively, k represents the crustal stiffness, which can be obtained by $k = G/H$ (here, $G = 10$

GPa) (Marone et al., 1991), and H represents the thickness of the velocity-strengthening zone, which were set to 6 km and 10 km for the shallow and deep region of the seismogenic fault, respectively. The frictional parameters $a-b$ of each sub-fault with cumulative slip $>0.05 \text{ m}$ in postseismic based on the above assumptions is shown in Fig. 2c. The values of $a-b$ on the seismogenic fault were in the range of $10^{-4}-2 \times 10^{-3}$ as a whole. The value of the $a-b$ in the shallow region was larger than that of the deep region of the seismogenic fault. The frictional parameter was positively correlated with deformation velocity according to the rate-and-state friction laws, which revealed the rapid afterslip in the near-field.

For the different characteristics of the kinematic afterslip and stress-driven afterslip distribution in the shallow region, the coseismic slip serves as the source model for the stress-driven afterslip simulation, and default that the afterslip is located on the coseismic Coulomb stress loading region. As the shallow part of the seismogenic fault represented Coulomb stress shadow (Fig. 2d), the stress driven afterslip was non-existent in the shallow upper crust. The near-field postseismic deformation may be caused by poroelastic rebound and afterslip, while the poroelastic rebound simulation cannot recovered the near-field deformation (Fig. 4).

The shallow upper crust slip was distributed in both the coseismic and postseismic periods, and two scenarios can explain this phenomenon. The first scenario is the small positive value of frictional parameter $a - b$, which allows the dynamic rupture to propagate across the velocity-strengthening area (Thomas et al., 2014), > 80% probability that the rupture can propagates across the velocity-strengthening area with the $a - b < 0.002$. The value of the frictional parameter $a - b$ in the shallow region was ~0.002, which was consistent with that of the models. The second scenario is that rapid shear heating allows the rate-strengthening area to generate large coseismic slip (Noda and Lapusta, 2013). The flash rupture and pore fluid thermal pressurization can increase the temperature to several hundreds of degrees (Rice, 2006), and

the rate-weakening and -strengthening frictional properties can be interconvertible under high temperature (Thomas et al., 2017; velocity-strengthening at 150–250 °C, velocity-weakening at 250–370 °C, and velocity-strengthening at >380 °C). Hence, the rate-strengthening area may convert to rate-weakening and then convert to rate-strengthening due to the shear heating. In addition to the above evidence, the velocity structure of the seismogenic fault based on the P-wave traveling data represents noticeable inhomogeneity and segmentation with depth (Wu et al., 2022). A low velocity zone was laterally distributed in the shallow upper crust (0–2 km), indicating high permeability water-bearing loose sediments. The dilatation region of the supershear segment may facilitate the inflow of pore fluid; further, the effective normal stress was reduced, leading to a drop of shear resistance. The relatively low frictional strength of the loose sediment may promote a decrease in the friction coefficient due to the rapid shear. Hence, shallow coseismic slip was mainly caused by the dynamic weakening in the coseismic period and continues to slip in the postseismic period.

3.3. Fault geometry controlling the deformation pattern

Many studies suggested that the fault geometry can control the segmentation of coseismic slip and reduce the coseismic displacement in the bending region (Manighetti et al., 2015; Klinger, 2010). However, the influence of the fault geometry for the postseismic deformation was still lacking. To evaluate the relationship between the fault geometry and the deformation pattern, we compiled the observations (fault strike, coseismic deformation, postseismic deformation, dilatation strain) and models (coseismic slip, postseismic slip) with 20 m buffer zone along the rupture (Fig. 6).

First, in EW direction, the coseismic deformation showed ~2 m on both sides and decreased to ~1 m on the bending region. The heterogeneous distributions of strain and NS deformation, including the compression strain (-2×10^{-5}) and NS motion (~80 cm) in the two bending regions (Liu et al., 2022), the dilatation strain (2×10^{-5}) in-between region, revealed a compressive stress regime on both sides of the bending region. Laboratory experiment showed that in the progress of the rupture propagation, the rupture trace deviated when the fault geometry changes under compression stress state (Templeton et al., 2009). The EW and NS coseismic deformation indicated that the fault bend hindered the slip propagation and reduced the magnitude of the

deformation.

Second, the shallow afterslip was mainly distributed in the bending region (Fig. 7), indicating that the stress release insufficiently at the compression region during coseismic period. Therefore, the unreleased stress should keep driving the extra afterslip during the postseismic period. The similar deformation pattern also observed in other strike-slip event, such as the 2019 Mw 7.1 Ridgecrest earthquake (Wang and Bürgmann, 2020), the 2003 Mw 7.2 Altai earthquake (Barbot et al., 2008) and 2001 Mw 7.8 Kokoxili earthquake (Zhao et al., 2018), where the near-field postseismic deformation was mainly distributed in the bending region. We simulated the slip model of the plane fault and bending fault to explored the influence of the fault geometry on the stress propagation and distribution. The two slip models set up the same slip distribution and fault parameter, and observed the static Coulomb stress change after the earthquake on fault plane. The obvious Coulomb stress loading in the bending region in the shallow portion of the fault, the value was ~5.5 MPa (Fig. 9a) and ~5 MPa (Fig. 9b) for the bending fault and plane fault respectively. The loading stress of the bending fault was ~10% higher than the plane fault, which indicated the bending region can accumulated more stress after the coseismic.

Third, the supershear rupture generally occurred on the simple geometry of the seismogenic fault (Bouchon et al., 2010), and the rupture velocity typically reduced upon encounter with the complex fault geometry such as bending, branching, or step-over (Harris et al., 2002; Poliakov et al., 2002; Aochi and Madariaga, 2003; Templeton et al., 2009). The fault strike changed drastically in the west side of the epicenter, whereas it changed gently in the supershear area (Fig. 6). The time-distance plot of the high-frequency sources also showed obvious discontinuity and decreased of the rupture velocity in the bending region [Fig. 8, modified from Zhang et al., 2022], which indicated that the difference of the fault geometry controls rupture-velocity variations between the east and west side of the epicenter and leads to changes in the stress propagation. We set up the bending fault was the receiver fault, and the other fault was the source fault to observe the static Coulomb stress distribution (Fig. S10c). The obvious shadow normal stress (clamp) was located on the bending region (Fig. 9c), the large shadow normal stress will increase the shear resistance and inhibit the rupture propagation. Therefore, the fault geometry controlled the rupture velocity and near-field postseismic deformation of the Maduo earthquake.

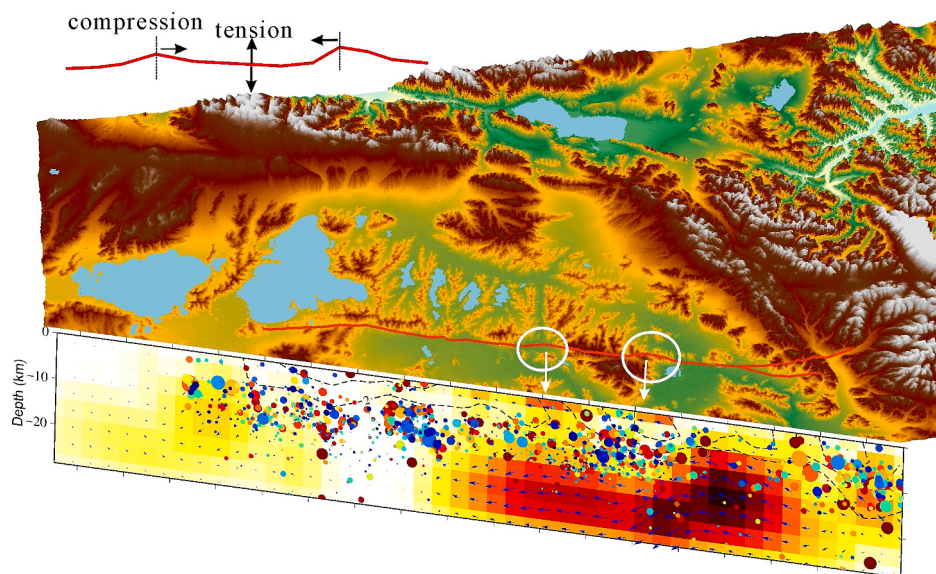


Fig. 7. Postseismic slip distribution of Maduo earthquake in three-dimensional map. The red line represents the rupture surface trace, the white ellipses represent the geometric bend of the fault. The colored circles denote the relocated aftershocks. The dashed contour lines indicate the coseismic slip. (For interpretation of the references to colour in this figure legend, the reader is referred to the web version of this article.)

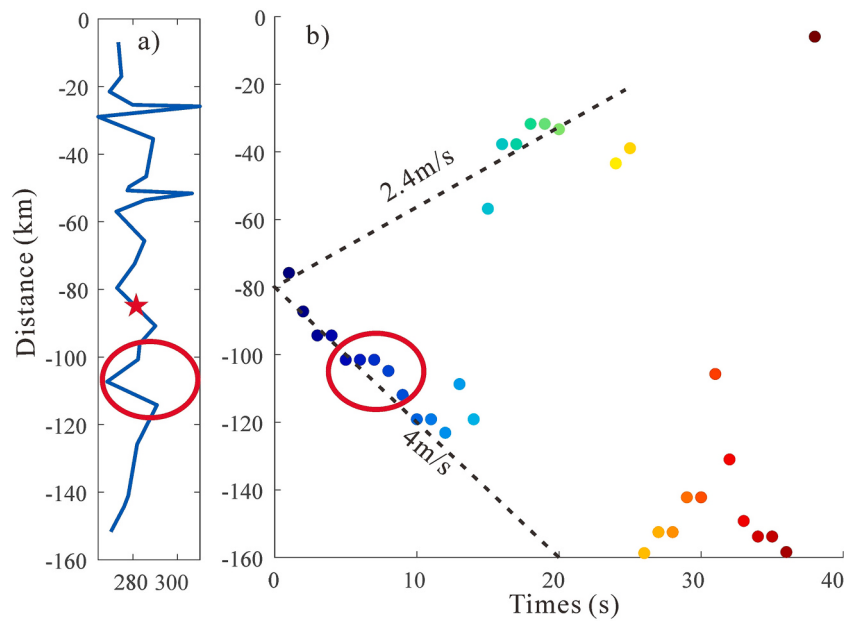


Fig. 8. Time-distance plot of the back-projection result. Modified from Zhang et al. (2022). The red oval represents the bending region. The red star represents the epicenter. The red ellipse indicates the bending region. The colour-code circles represent the high-frequency sources. (For interpretation of the references to colour in this figure legend, the reader is referred to the web version of this article.)

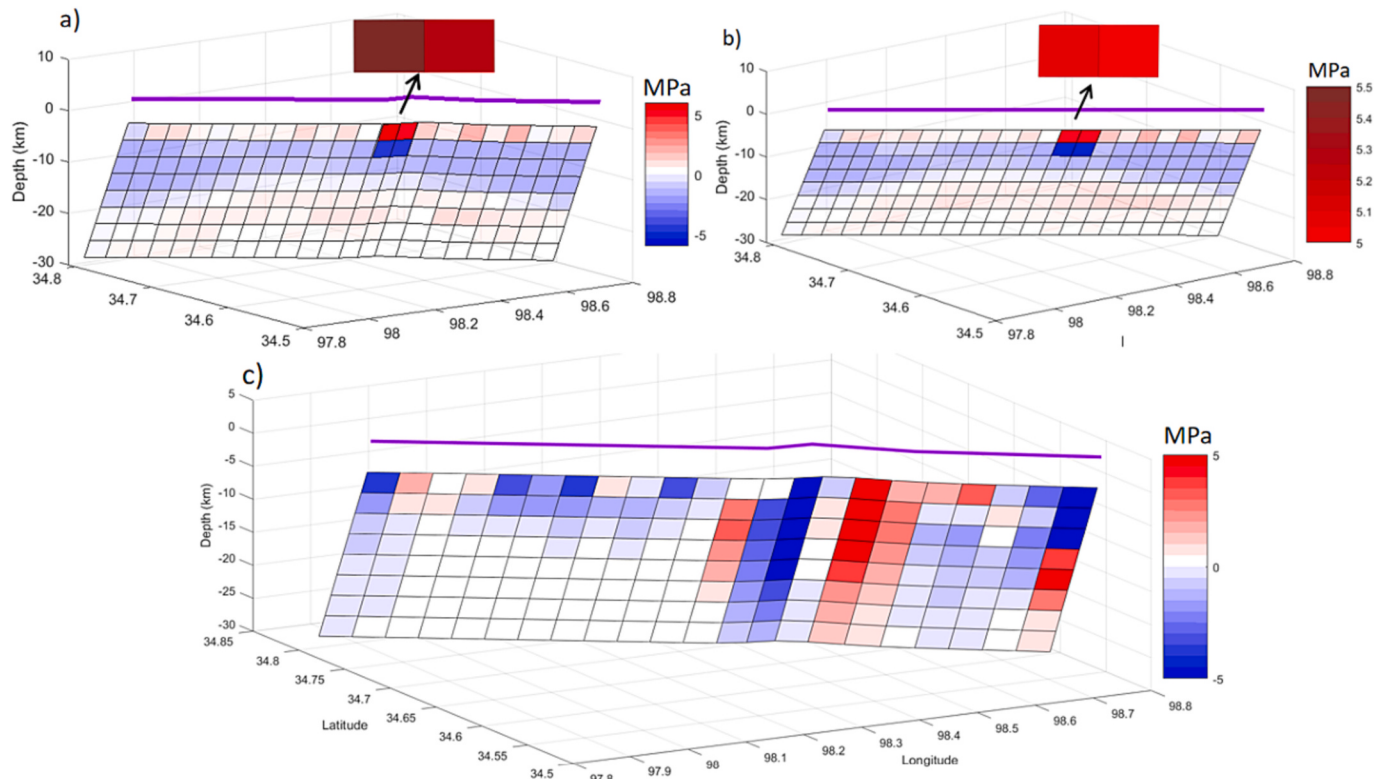


Fig. 9. Coulomb stress change of different fault geometry. a) Coulomb stress change on the fault with bending structure. b) Coulomb stress change on the plane fault. c) Normal stress change when the fault with bending structure as receiver fault. The purple line represents the fault trace. (For interpretation of the references to colour in this figure legend, the reader is referred to the web version of this article.)

4. Conclusion

In this study, we processed ~0.85 yr postseismic deformation of the Maduo earthquake to investigate the fault frictional property and mechanism of deformation pattern. The significant near-field

deformation in the bending region, and the complex fault geometry highlights that the fault bending could control both coseismic and postseismic deformation pattern. The near and far-field postseismic deformation patterns indicate different decay velocities, which reflect the varying frictional properties of the seismogenic fault. Both the

moderate value of the rate-and-state parameter $a - b$ for the overlapped area in the shallow region (~ 0.002) and the shear heating of the rapid rupture allow the dynamic rupture to propagate across the rate-strengthening area. Therefore, the bending fault geometry, the varying frictions, and rupture dynamics influence the patterns of stress propagation and surface deformation, which is worth noting in evaluating seismic risks on other strike-slip faults in the Bayan Har block.

CRediT authorship contribution statement

Lei Zhao: Writing – original draft, Methodology, Conceptualization. **Wenbin Xu:** Writing – review & editing, Methodology. **Lei Xie:** Software, Data curation. **Dezheng Zhao:** Validation, Investigation. **Zhihui Zhu:** Resources, Investigation. **Pingping Wu:** Validation, Software. **Huili Guo:** Software, Data curation.

Declaration of Competing Interest

None.

Data availability

The Sentinel-1 SAR data used in this study are copyrighted by the European Space Agency and additionally distributed by the Alaska Satellite Facility Distributed Active Archive Center (<https://vertex.daac.asf.alaska.edu>).

Acknowledgement

We would like to thank the European Space Agency for providing Sentinel-1A data. This work was supported by the National Natural Science Foundation of China (42174023), Frontier cross research project of Central South University (Grant number: 2023QYJC006). The figures were prepared using the public domain Generic Mapping Tools and MATLAB. Thank you for Han Yue provides the coseismic slip model. Comments and suggestions by Editor Chief Ling Chen and three anonymous reviewers helped improve this manuscript.

Appendix A. Supplementary data

Supplementary data to this article can be found online at <https://doi.org/10.1016/j.tecto.2023.230000>.

References

- Aochi, H., Madariaga, R., 2003. The 1999 Izmit, Turkey, earthquake: nonplanar fault structure, dynamic rupture process, and strong ground motion. *Bull. Seismol. Soc. Am.* 93 (3), 1249–1266. <https://doi.org/10.1785/0120020167>.
- Avouac, J.P., 2015. From geodetic imaging of seismic and aseismic fault slip to dynamic modeling of the seismic cycle. *Annu. Rev. Earth Planet. Sci.* 43, 233–271. <https://doi.org/10.1146/annurev-earth-060614-105302>.
- Barbot, S., Hamiel, Y., Fialko, Y., 2008. Space geodetic investigation of the coseismic and postseismic deformation due to the 2003 Mw7.2 Altai earthquake: Implications for the local lithospheric rheology. *J. Geophys. Res. Solid Earth* 113 (B3). <https://doi.org/10.1029/2007JB005063>.
- Barbot, S., Fialko, Y., Bock, Y., 2009. Postseismic deformation due to the Mw 6.0 2004 Parkfield earthquake: Stress-driven creep on a fault with spatially variable rate-and-state friction parameters. *J. Geophys. Res. Solid Earth* 114 (B7). <https://doi.org/10.1029/2008JB005748>.
- Bevis, M., Pan, E., Zhou, H., Han, F., Zhu, R., 2015. Surface deformation due to loading of a layered elastic half-space: constructing the solution for a general polygonal load. *Acta Geophys.* 63, 11944–11948. <https://doi.org/10.1515/acgeo-2015-0034>.
- Bouchon, M., Karabulut, H., Bouin, M.P., Schmittbuhl, J., Vallée, M., Archuleta, R., Marsan, D., 2010. Faulting characteristics of supershear earthquakes. *Tectonophysics* 493 (3–4), 244–253. <https://doi.org/10.1016/j.tecto.2010.06.011>.
- Chen, K., Avouac, J.P., Geng, J., Liang, C., Zhang, Z., Li, Z., Zhang, S., 2022. The 2021 Mw 7.4 Madou Earthquake: An Archetype Bilateral Slip-Pulse Rupture arrested at a Splay Fault. *Geophys. Res. Lett.* 49 (2) <https://doi.org/10.1029/2021GL095243> e2021GL095243.
- Chorsi, T.S., Braumiller, J., Deng, F., Dixon, T.H., 2022. Afterslip from the 2020 M 6.5 Monte Cristo Range, Nevada Earthquake. *Geophys. Res. Lett.* e2022GL099952 <https://doi.org/10.1029/2022GL099952>.
- Dogan, U., Demir, D.Ö., Çakır, Z., Ergintav, S., Ozener, H., Akoğlu, A.M., Reilinger, R., 2014. Postseismic deformation following the Mw 7.2, 23 October 2011 Van earthquake (Turkey): evidence for aseismic fault reactivation. *Geophys. Res. Lett.* 41 (7), 2334–2341. <https://doi.org/10.1002/2014GL059291>.
- Fialko, Y., Sandwell, D., Simons, M., Rosen, P., 2005. Three-dimensional deformation caused by the 2003 Bam, Iran, earthquake and the origin of shallow slip deficit. *Nature* 435 (7040), 295–299. <https://doi.org/10.1038/nature03425>.
- Goldstein, R.M., Werner, C.L., 1998. Radar interferogram filtering for geophysical applications. *Geophys. Res. Lett.* 25 (21), 4035–4038. <https://doi.org/10.1029/1998GL900033>.
- Harris, R.A., Dolan, J.F., Hartleb, R., Day, S.M., 2002. The 1999 Izmit, Turkey, earthquake: a 3D dynamic stress transfer model of intraearthquake triggering. *Bull. Seismol. Soc. Am.* 92 (1), 245–255. <https://doi.org/10.1785/0120000825>.
- He, L., Feng, G., Wu, X., Lu, H., Xu, W., Wang, Y., Li, Z., 2021. Coseismic and early postseismic slip models of the 2021 Mw 7.4 Madou earthquake (western China) estimated by space-based geodetic data. *Geophys. Res. Lett.* 48 (24) <https://doi.org/10.1029/2021GL095860> e2021GL095860.
- Jin, Z., Fialko, Y., 2021. Coseismic and early postseismic deformation due to the 2021 M7.4 Madou (China) earthquake. *Geophys. Res. Lett.* 48 (21) <https://doi.org/10.1029/2021GL095213> e2021GL095213.
- Klinger, Y., 2010. Relation between continental strike-slip earthquake segmentation and thickness of the crust. *J. Geophys. Res. Solid Earth* 115 (B7), 2010. <https://doi.org/10.1029/2009JB006550>.
- Li, C., Li, T., Shan, X., Zhang, G., 2023. Extremely large off-fault deformation during the 2021 mw 7.4 Madou, Tibetan Plateau, Earthquake. *Seismol. Res. Lett.* 94 (1), 39–51.
- Li, C., Zhang, G., Shan, X., Zhao, D., Song, X., 2020. Geometric variation in the surface rupture of the 2018 mw7.5 Palu earthquake from subpixel optical image correlation. *Remote Sens.* 12 (20), 3436. <https://doi.org/10.3390/rs12203436>.
- Liu, J., Hu, J., Li, Z., Ma, Z., Wu, L., Jiang, W., Zhu, J., 2022. Complete three-dimensional coseismic displacements due to the 2021 Madou earthquake in Qinghai Province, China from Sentinel-1 and ALOS-2 SAR images. *Sci. China Earth Sci.* 65 (4), 687–697. <https://doi.org/10.1007/s11430-021-9868-9>.
- Liu-Zeng, J., Yao, W., Liu, X., Shao, Y., Wang, W., Han, L., Tu, H., 2022. High-resolution structure-from-motion models covering 160 km-long surface ruptures of the 2021 MW 7.4 Madou earthquake in northern Qinghai-Tibetan Plateau. *Earthquake Res. Adv.* 100140 <https://doi.org/10.1016/j.eqrea.2022.100140>.
- Manighetti, I., Caulet, C., De Barros, L., Perrin, C., Cappa, F., Gaudemer, Y., 2015. Generic along-strike segmentation of a far normal faults, E ast a frica: implications on fault growth and stress heterogeneity on seismogenic fault planes. *Geochem. Geophys. Geosyst.* 16 (2), 443–467. <https://doi.org/10.1002/2014GC005691>.
- Marone, C.J., Scholtz, C.H., Bilham, R., 1991. On the mechanics of earthquake afterslip. *J. Geophys. Res. Solid Earth* 96 (B5), 8441–8452. <https://doi.org/10.1029/91JB00275>.
- Melgar, D., Geng, J., Crowell, B.W., Haase, J.S., Bock, Y., Hammond, W.C., Allen, R.M., 2015. Seismogeodesy of the 2014 Mw6.1 Napa earthquake, California: Rapid response and modeling of fast rupture on a dipping strike-slip fault. *J. Geophys. Res. Solid Earth* 120 (7), 5013–5033. <https://doi.org/10.1002/2015JB011921>.
- Miyazaki, S.I., Segall, P., Fukuda, J., Kato, T., 2004. Space time distribution of afterslip following the 2003 Tokachi-oki earthquake: Implications for variations in fault zone frictional properties. *Geophys. Res. Lett.* 31 (6).
- Morishita, Y., Lazecky, M., Wright, T.J., Weiss, J.R., Elliott, J.R., Hooper, A., 2020. LiCSBAS: an open-source InSAR time series analysis package integrated with the LiCSBAS automated Sentinel-1 InSAR processor. *Remote Sens.* 12 (3), 424. <https://doi.org/10.3390/rs12030424>.
- Noda, H., Lapusta, N., 2013. Stable creeping fault segments can become destructive as a result of dynamic weakening. *Nature* 493 (7433), 518–521. <https://doi.org/10.1038/nature11703>.
- Pan, J., Bai, M., Li, C., Liu, F., Li, H., Liu, D., Marie-, Luce C., Wu, K., Wang, P., Lu, H., Chen, P., Li, C., 2021. Coseismic surface rupture and seismogenic structure of the 2021-05-22 Madou (Qinghai) MS7.4 earthquake. *Acta Geol. Sin.* 95 (6), 1655–1670.
- Poliakov, A.N.B., Dmowska, R., Rice, J.R., 2002. Dynamic shear rupture interactions with fault bends and off-axis secondary faulting. *J. Geophys. Res. Solid Earth* 107 (B11). <https://doi.org/10.1029/2001JB000572>. ESE 6-1-ESE 6-18.
- Rice, J.R., 2006. Heating and weakening of faults during earthquake slip. *J. Geophys. Res. Solid Earth* 111 (B5). <https://doi.org/10.1029/2005JB004006>.
- Scholz, C.H., 2002. *The Mechanics of Earthquakes and Faulting*. Cambridge university press.
- Templeton, E.L., Baudet, A., Bhat, H.S., Dmowska, R., Rice, J.R., Rosakis, A.J., Rousseau, C.E., 2009. Finite element simulations of dynamic shear rupture experiments and dynamic path selection along kinked and branched faults. *J. Geophys. Res. Solid Earth* 114 (B8). <https://doi.org/10.1029/2008JB006174>.
- Thomas, M.Y., Lapusta, N., Noda, H., Avouac, J.P., 2014. Quasi-dynamic versus fully dynamic simulations of earthquakes and aseismic slip with and without enhanced coseismic weakening. *J. Geophys. Res. Solid Earth* 119 (3), 1986–2004. <https://doi.org/10.1002/2013JB010615>.
- Thomas, M.Y., Avouac, J.P., Lapusta, N., 2017. Rate-and-state friction properties of the Longitudinal Valley Fault from kinematic and dynamic modeling of seismic and aseismic slip. *J. Geophys. Res. Solid Earth* 122 (4), 3115–3137.
- Wallace, L.M., Hreinsdóttir, S., Ellis, S., Hamling, I., D'Anastasio, E., Denys, P., 2018. Triggered slow slip and afterslip on the southern Hikurangi subduction zone following the Kaikōura earthquake. *Geophys. Res. Lett.* 45 (10), 4710–4718. <https://doi.org/10.1029/2018GL077385>.
- Wang, K., Bürgmann, R., 2020. Co- and early postseismic deformation due to the 2019 Ridgecrest earthquake sequence constrained by Sentinel-1 and COSMO-SkyMed SAR data. *Seismol. Res. Lett.* 91 (4), 1998–2009. <https://doi.org/10.1785/0220190299>.

- Wang, R., Kümpel, H.J., 2003. Poroelasticity: Efficient modeling of strongly coupled, slow deformation processes in a multilayered half-space. *Geophysics* 68 (2), 705–717. <https://doi.org/10.1190/1.1567241>.
- Wang, M., Shen, Z.K., 2020. Present-day crustal deformation of continental China derived from GPS and its tectonic implications. *J. Geophys. Res. Solid Earth* 125 (2). <https://doi.org/10.1029/2019JB018774> e2019JB018774.
- Wang, R., Parolai, S., Ge, M., Jin, M., Walter, T., Zschau, J., 2013. The 2011 Mw 9.0 Tohoku earthquake: comparison of GPS and strong-motion data. *Bull. Seismol. Soc. Am.* 103 (2 B), 1336–1347. <https://doi.org/10.1785/0120110264>.
- Wang, W., Fang, L., Wu, J., Tu, H., Chen, L., Lai, G., Zhang, L., 2021. Aftershock sequence relocation of the 2021 Ms7. 4 Maduo earthquake, Qinghai, China. *Sci. China Earth Sci.* 64 (8), 1371–1380. <https://doi.org/10.1007/s11430-021-9803-3>.
- Wang, S., Song, C., Li, S., Li, X., 2022. Resolving co-and early post-seismic slip variations of the 2021 M W 7.4 Maduo earthquake in east Bayan Har block with a block-wide distributed deformation mode from satellite synthetic aperture radar data. *Earth Planet. Phys.* 6 (1), 108–122. <https://doi.org/10.26464/ep2022007>.
- Werner, C., Wegmüller, U., Strozzi, T., Wiesmann, A., 2000. October. Gamma SAR and interferometric processing software. In: Proceedings of the ers-envisat symposium, Gothenburg, Sweden, 1620, p. 1620.
- Wu, P., Chang, L., Lu, L., Guo, H., Lv, M., Ding, Z., 2022. Three-dimensional fine velocity structure of the upper crust of the 2021 Madoi MS7.4 earthquake, Qinghai. *Chinese J. Geophys.* 65 (6), 2006–2021. <https://doi.org/10.6038/cjg2022P0860>.
- Xiong, W., Chen, W., Wang, D., Wen, Y., Nie, Z., Liu, G., Zhao, B., 2022. Coseismic slip and early afterslip of the 2021 Mw 7.4 Maduo, China earthquake constrained by GPS and InSAR data. *Tectonophysics* 840, 229558. <https://doi.org/10.1016/j.tecto.2022.229558>.
- Xu, G., Xu, C., Wen, Y., Xiong, W., Valkaniotis, S., 2020. The complexity of the 2018 Kaktovik earthquake sequence in the northeast of the Brooks Range, Alaska. *Geophys. Res. Lett.* 47 (19) <https://doi.org/10.1029/2020GL088012> e2020GL088012.
- Yamanaka, Y., Kikuchi, M., 2004. Asperity map along the subduction zone in northeastern Japan inferred from regional seismic data. *J. Geophys. Res. Solid Earth* 109 (B7).
- Yuan, Z., Li, T., Su, P., Sun, H., Ha, G., Guo, P., Thompson Jobe, J., 2022. Large surface-rupture gaps and low surface fault slip of the 2021 Mw 7.4 Maduo earthquake along a low-activity strike-slip fault, Tibetan Plateau. *Geophys. Res. Lett.* 49 (6) <https://doi.org/10.1029/2021GL096874> e2021GL096874.
- Yue, H., Shen, Z.K., Zhao, Z., Wang, T., Cao, B., Li, Z., Xue, L., 2022. Rupture process of the 2021 M7. 4 Maduo earthquake and implication for deformation mode of the Songpan-Ganzi terrane in Tibetan Plateau. *Proc. Natl. Acad. Sci.* 119 (23), e2116445119 <https://doi.org/10.1073/pnas.2116445119>.
- Zhang, X., Feng, W., Du, H., Samsonov, S., Yi, L., 2022. Supershear rupture during the 2021 MW 7.4 Maduo, China, earthquake. *Geophys. Res. Lett.* 49 (6) <https://doi.org/10.1029/2022GL097984> e2022GL097984.
- Zhao, D., Qu, C., Shan, X., Zuo, R., Liu, Y., Gong, W., Zhang, G., 2018. Broadscale postseismic deformation and lower crustal relaxation in the central Bayankala Block (central Tibetan Plateau) observed using InSAR data. *J. Asian Earth Sci.* 154, 26–41. <https://doi.org/10.1016/j.jseas.2017.12.016>.
- Zhao, D., Qu, C., Chen, H., Shan, X., Song, X., Gong, W., 2021. Tectonic and geometric control on fault kinematics of the 2021 Mw7. 3 Maduo (China) earthquake inferred from interseismic, coseismic, and postseismic InSAR observations. *Geophys. Res. Lett.* 48 (18) <https://doi.org/10.1029/2021GL095417> e2021GL095417.
- Zhou, Y., Parsons, B.E., Walker, R.T., 2018a. Characterizing complex surface ruptures in the 2013 M w 7.7 Balochistan earthquake using three-dimensional displacements. *J. Geophys. Res. Solid Earth* 123 (11), 10,191–10,211. <https://doi.org/10.1029/2018JB016043>.
- Zhou, Y., Thomas, M.Y., Parsons, B., Walker, R.T., 2018b. Time-dependent postseismic slip following the 1978 Mw 7.3 Tabas-e-Golshan, Iran earthquake revealed by over 20 years of ESA InSAR observations. *Earth Planet. Sci. Lett.* 483, 64–75. <https://doi.org/10.1016/j.epsl.2017.12.005>.